Dynamic recrystallization mechanisms and twining evolution during hot deformation of Inconel 718

M. Azarbarmas, M. Aghaie-Khafri, J.M. Cabrera, J. Calvo

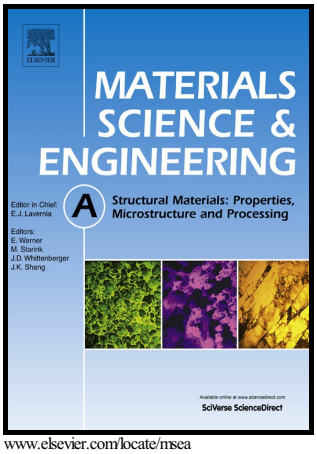

www.elsevier.com/locate/msea

PII: S0921-5093(16)31182-0
DOI: http://dx.doi.org/10.1016/j.msea.2016.09.100
Reference: MSA34185

To appear in: *Materials Science & Engineering A*

Received date: 3 March 2016
Revised date: 20 September 2016
Accepted date: 25 September 2016

Cite this article as: M. Azarbarmas, M. Aghaie-Khafri, J.M. Cabrera and J Calvo, Dynamic recrystallization mechanisms and twining evolution during hc deformation of Inconel 718, *Materials Science & Engineering A* http://dx.doi.org/10.1016/j.msea.2016.09.100

Dynamic recrystallization mechanisms and twining evolution during hot deformation of Inconel 718

M. Azarbarmas[a], M. Aghaie-Khafri[a*], J.M. Cabrera[b], J. Calvo[b]

[a] Faculty of Materials Science and Engineering, K.N. Toosi University of Technology, Postal Code: 1999143344, Tehran, Iran

[b] Departament de Ciència dels Materials i Enginyeria Metal·lúrgica, ETSEIB – Universitat Politècnica de Catalunya, Av. Diagonal 647, 08028 Barcelona, Spain

[*]Corresponding author. maghaei@kntu.ac.ir

Abstract

The hot deformation behavior of an IN718 superalloy was studied by isothermal compression tests under the deformation temperature range of 950-1100 °C and strain rate range of 0.001-1 s^{-1} up to true strains of 0.05, 0.2, 0.4 and 0.7. Electron backscattered diffraction (EBSD) technique was employed to investigate systematically the effects of strain, strain rate and deformation temperature on the subgrain structures, local and cumulative misorientations and twinning phenomena. The results showed that the occurrence of dynamic recrystallization (DRX) is promoted by increasing strain and deformation temperature and decreasing strain rate. The microstructural changes showed that discontinuous dynamic recrystallization (DDRX), characterized by grain boundary bulging, is the dominant nucleation mechanism in the early stages of deformation in which DRX nucleation occurs by twining behind the bulged areas. Twin boundaries of nuclei lost their $\sum 3$ character with further deformation. However, many simple and multiple twins can be also regenerated during the growth of grains. The results showed that

continuous dynamic recrystallization (CDRX) is promoted at higher strains and large strain rates, and lower temperatures, indicating that under certain conditions both DDRX and CDRX can occur simultaneously during the hot deformation of IN718.

Keywords: Inconel 718; Hot compression test; EBSD; Misorientation; Twinning

1. **Introduction**

Inconel 718 is a typical Ni-based superalloy having high strength [1], excellent resistance to oxidation [2], high corrosion resistance [3,4], adequate ductility and toughness [5], favorable weldability [6] and good machining performance [7]. IN718 is used for critical parts in modern aero-engines, extrusion dies and gas-turbines [8–17]. Hot deformation is necessary to achieve the required properties in IN718. This is the reason why the hot deformation behavior of IN718 has been widely studied over the past decade [7,18–20].

Generally, dynamic recovery and dynamic recrystallization (DRX) are competitive restoration mechanisms during the hot deformation of alloys. IN718 is a relatively low stacking fault energy material [21], and consequently, DRX is believed to be the main restoration process that controls the microstructure evolution of IN718 during hot working. There are numerous works in the literature which have explored the parameters affecting DRX on IN718 [22–29].

There is an agreement in the literature in considering two main mechanisms for DRX [30,31], namely discontinuous dynamic recrystallization (DDRX) and continuous dynamic recrystallization (CDRX). DDRX is characterized by nucleation and growth of the nuclei through a bulging mechanism [32,33], while CDRX is characterized by transforming dislocation cell boundaries into low-angle subgrain boundaries and then into high-angle boundaries [34,35], and consequently cannot be considered as a mechanism that is controlled by nucleation

and growth. Recently, Lin et al.[36] studied the DRX behavior of a nickel-based superalloy, and concluded that DDRX plays a dominant role during the nucleation stage of DRX. Jiang et al. [37] reported the same behavior for a 617B alloy during hot compression tests. Guo et al. [38] showed that DDRX was promoted by increasing the deformation temperature in an Inconel 625 superalloy. Similar results have been reported by Wang [23], who observed that decreasing the deformation temperature promotes the effect of CDRX in a superalloy 718. Cao et al. [39] investigated the effects of processing parameters on the DRX behavior of a 800H alloy, and showed that twinning plays a significant role during the nucleation and growth of the recrystallized grains. The results obtained by Zhang et al. [40] demonstrated that the nucleation mechanisms of DDRX and CDRX can simultaneously occur in a nickel-based superalloy during hot deformation.

Although there are several works concerning the mechanisms of DRX nucleation in nickel-based alloys, further studies are still required to clarify the effects of processing parameters on these mechanisms and associated twining phenomena occurring at high temperature deformation of nickel-based superalloys. Consequently, the main goal of the present work is to carry out a systematic investigation on the influence of strain, strain rate and deformation temperature on the evolution of grain structure, substructure, twins, as well as nature and misorientation of the grain boundaries, to understand the nucleation mechanisms of DRX during the hot deformation of an IN718 superalloys using electron backscatter diffraction analysis.

2. Material and experimental procedures

The chemical composition of wrought IN71598 superalloy used in this investigation is listed in Table 1. The specimens were solution treated at 1025 °C for 1 h, followed by cold-water

quenching. The initial microstructure comprises equiaxed grains and annealing twins, as shown in Fig. 1. The presence of equiaxed grains and annealing twins shows that the initial material has a recrystallized structure [41,42]. The average grain size (without twins) was measured to be about 45 μm by the linear intercept method.

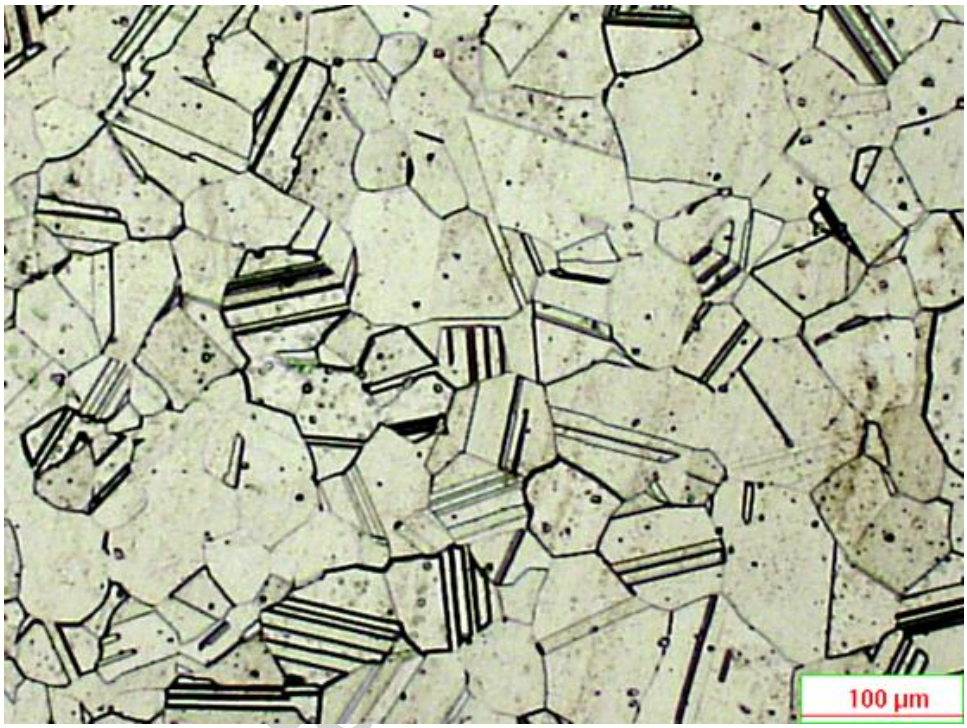

Fig. 1. Optical image of the studied IN718 before hot deformation.

Cylindrical compression specimens of 5 mm in diameter and 10 mm in height were machined from the annealed material. Isothermal compression tests were carried out in a Baehr DIL-805 deformation dilatometer. Compression tests were conducted to true strains of about 0.05, 0.2, 0.4 and 0.7 under different temperatures (950, 1000, 1050 and 1100 °C) and various strain rates (0.001, 0.01, 0.1 and 1 s^{-1}). A K-type thermocouple was spot-welded at the middle of the specimen to accurately control the heating and cooling rates and measuring the temperature of the specimen. Argon gas was utilized as the shielding and quenching gas in the machine. In order to minimize the friction and avoid the adhesion, a molybdenum foil with a thickness of 0.1

mm was used between the anvils and the specimen surface. However, it was necessary to use correction factors to eliminate the effect of interfacial friction. A simplified theoretical analysis of the barrel compression test for estimation of the friction factor was used to remove the friction effects. Details of this method can be found elsewhere [41,43].

Table 1. Chemical composition of the studied IN718 (wt.%)

Ni	Cr	Fe	Nb+Ta	Mo	Ti	Al	Co	Sl	Mn	Cu	C
54.00	18.21	17.29	5.35	2.98	0.91	0.66	0.24	0.08	0.07	0.07	0.03

The samples for EBSD evaluation were ground with SiC papers, mechanically polished with diamond paste, and then polished with 0.04 µm colloidal silica solution for one hour. A Zeiss UltraPlus analytical field emission gun scanning electron microscope equipped with an EBSD detector, provided by HKL Technology, was utilized for microstructural characterization purposes. EBSD maps were obtained with a step size of 0.25–1 µm depending on the grain size to be analyzed. HKL Channel 5 software was used for the EBSD data acquisition and analysis. In orientation imaging microscopy (OIM) maps, high angle boundaries (HABs), greater than 15°, and low angle boundaries (LABs), smaller than 15°, were represented by black lines and white lines, respectively, in the corresponding figures. Different colors were used for showing HABs with a coincidence site lattice (CSL) relationship. Σ3 twin boundaries are shown as red lines, while the Σ9 and Σ27 twin boundaries are displayed as yellow lines and green lines, respectively.

3. Results

3.1. Stress-strain curves

The friction corrected hot flow curves are presented in Fig. 2, which exhibits the effect of both temperature and strain rate on the softening processes of the present IN718 alloy. Fig. 2a

illustrates the stress-strain curves of samples compressed at a strain rate of 0.01 s−1 and different temperatures. Details of the friction-correction of flow curves have been reported elsewhere [43]. Typically, the flow stress increases to a maximum value (peak stress), and then decreases to an almost constant stress level (the steady state stress). The observed behavior is typical in alloys showing the occurrence of DRX during hot deformation [38,44–46]. Moreover, it is observed that the peak stress decreases as the temperature increases, which is a conventional behavior and consistent with other reports for nickel-based superalloys [47–50]. Flow curves of IN718 alloy obtained at the temperature of 1100 °C and at various strain rates from 0.001 to 1 s^{-1} are also displayed in Fig. 2b. It can be observed that the peak stress becomes more pronounced when the strain rate increases. Moreover, the peak stress decreases with decreasing strain rates. It is worth mentioning that the peak strain (the one associated to the peak stress) also decreases with decreasing strain rates. Peak strain is usually associated to the onset of DRX.

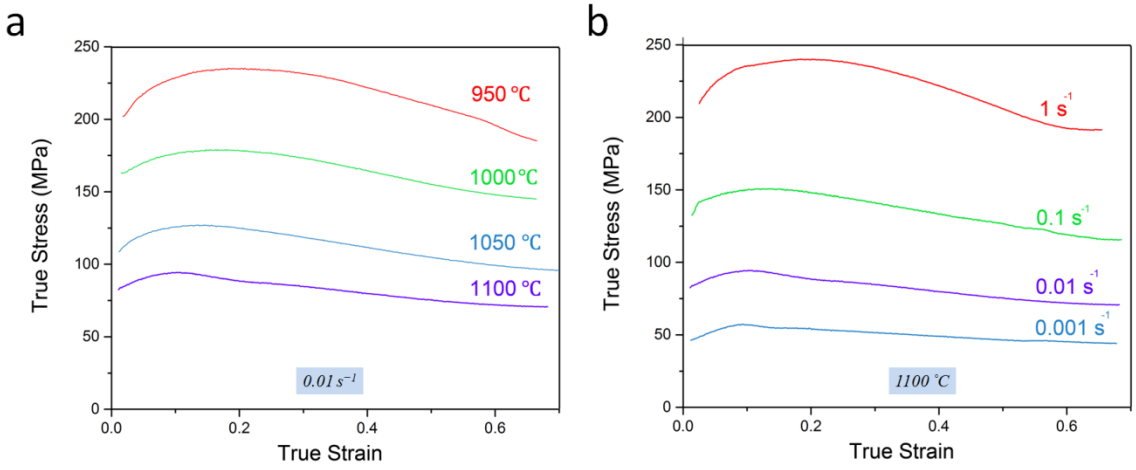

Fig. 2. True stress-true strain curves obtained by hot compression tests of IN718 samples at (a) strain rate of 0.01 s^{-1} and different temperatures and (b) temperature of 1100 °C and different strain rates.

3.2. Characteristic microstructures

The microstructures of the superalloy IN718 after compression at various temperatures, a strain rate of 1 s^{-1} and a strain of 0.7 are shown as OIM maps in Fig. 3. In this figure, the recrystallized grains, illustrated in blue, are distinguished from un-recrystallized ones through differences in the grain size and aspect ratio. It is evident that the fraction and size of the recrystallized grains are strongly dependent on the deformation temperature. At a temperature of 950 °C a few small recrystallized grains, having an equiaxed shape, are detectable. These grains are preferably formed at prior grain boundaries, leading to a necklace structure. By increasing the temperature, a higher fraction of bigger recrystallized grains appears in the structure.

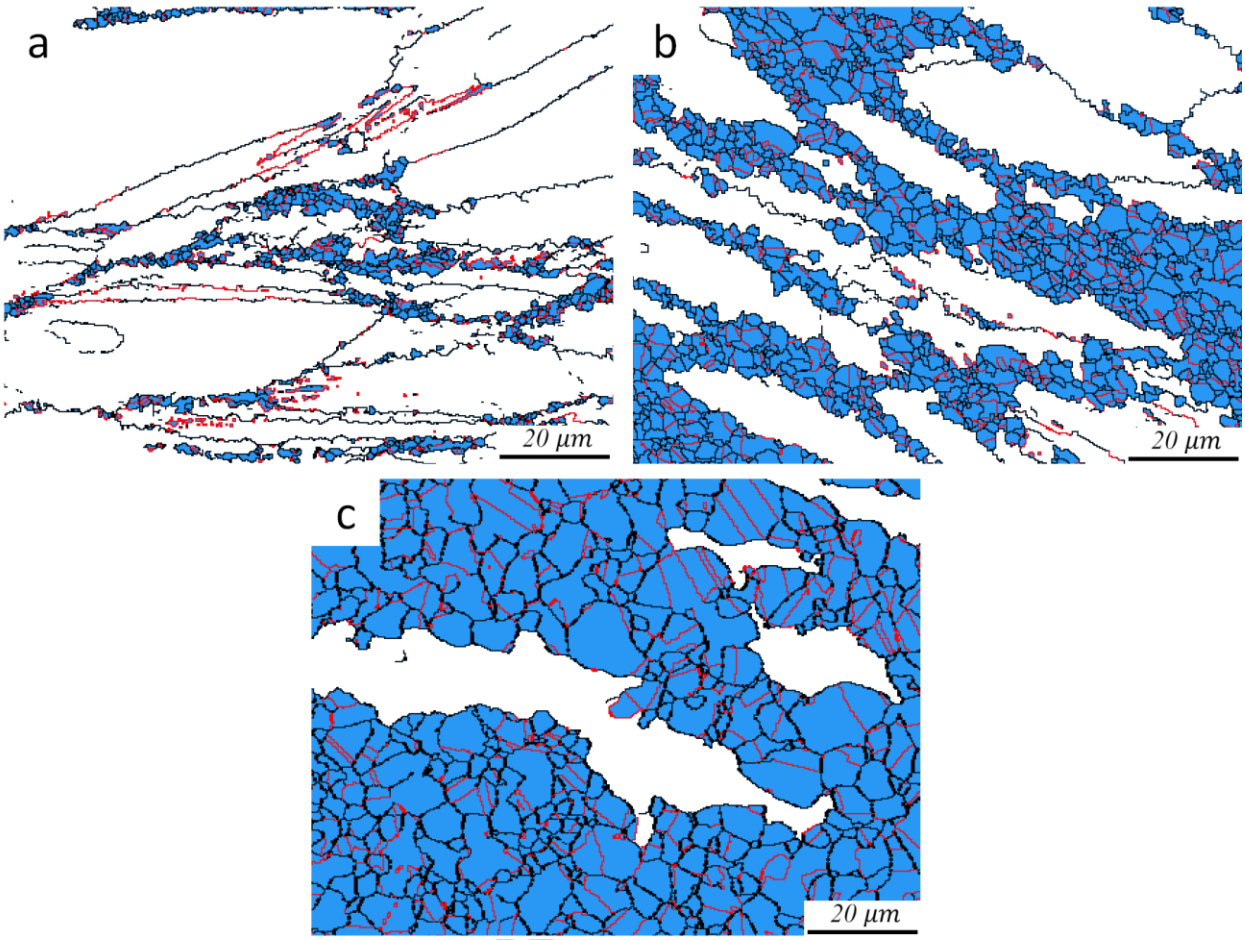

Fig. 3. OIM maps of IN718 sample deformed at strain rate of 0.1 s^{-1} and temperatures of (a) 950, (b) 1000 and (c) 1050 °C; the recrystallized grains are displayed with blue color.

Another important parameter affecting the recrystallization behavior is the strain rate. The effect of the strain rate is demonstrated by OIM maps in Fig. 4. These images include specimens compressed at a temperature of 1050 °C under strain rates of 0.01, 0.1 and 1 s^{-1}, to a strain of 0.7. It can be observed that the fraction and size of the DRX grains, shown in blue, decrease with increasing the strain rate.

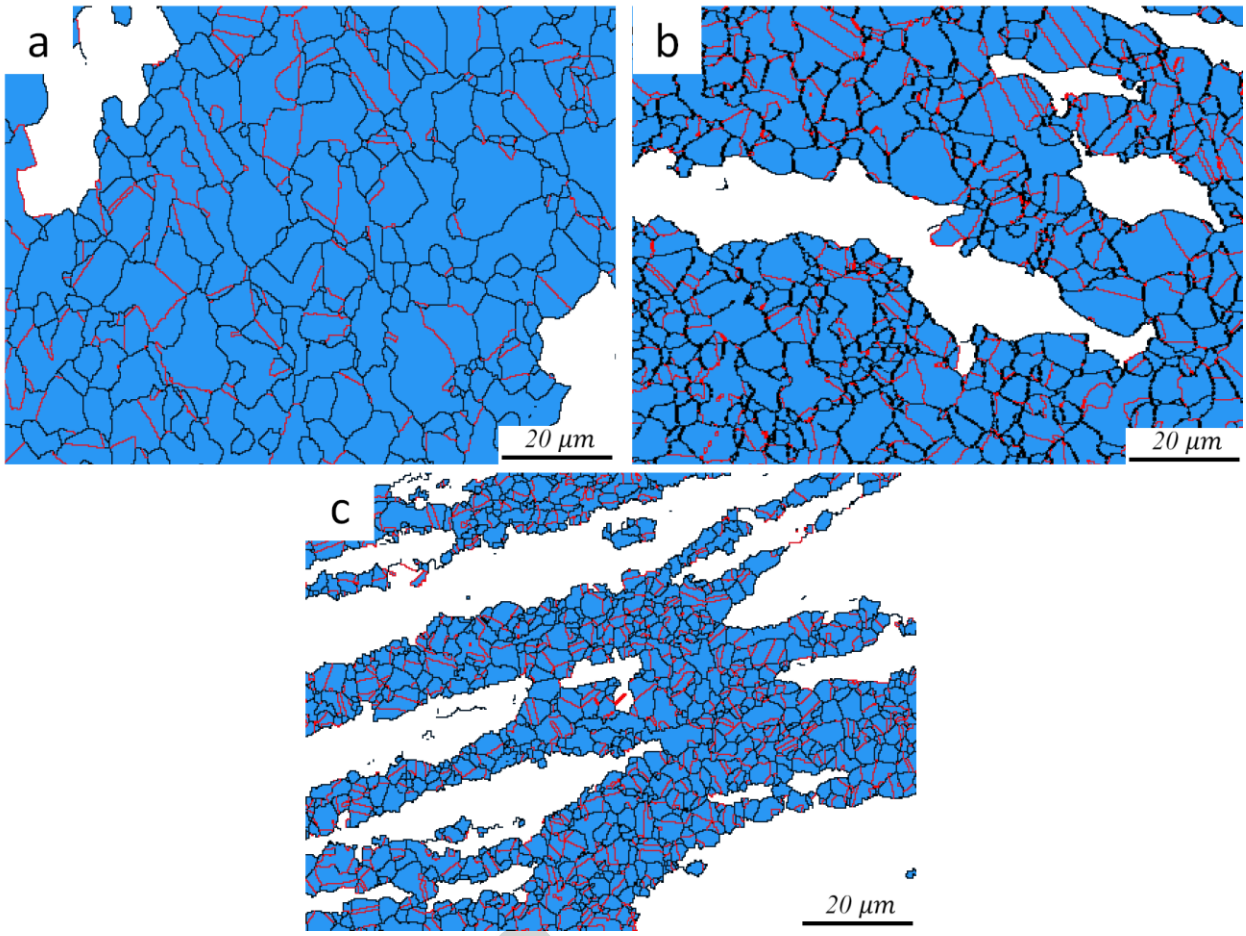

Fig. 4. OIM maps of IN718 samples deformed at temperatures of 1050 °C and strain rate of (a) 0.01, (b) 0.1 and (c) 1 s^{-1}; the recrystallized grains are exhibited with blue color.

3.3. Misorientation angle evolution

3.3.1. Effect of strain

Fig. 5 shows the influence of the strain on the OIM maps of the current IN718 deformed at 1100 °C and 0.1 s^{-1}. Under relatively low strain (0.05), well below the peak strain, the grain boundaries are considerably serrated, (this bulged boundaries can be observed in Fig. 5a marked by yellow arrows) and there is almost no DRX nucleus. It is also worth noting that LAGBs (see white boundaries in Fig 5a) are accumulated on the vicinity of old grain boundaries.

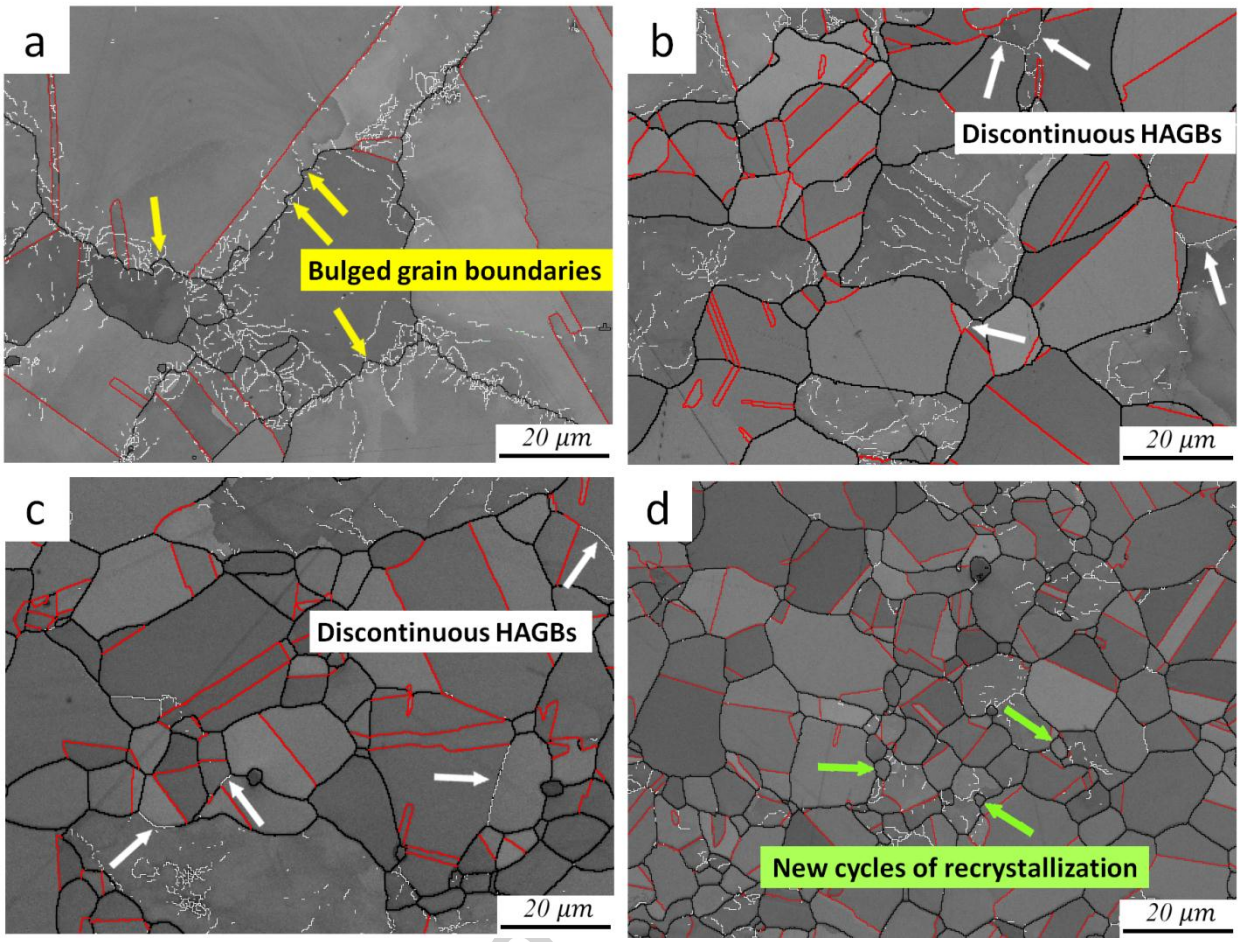

Fig. 5. OIM maps of IN718 samples deformed under 1100 °C and 0.1 s^{-1} at the strains of (a) 0.05, (b) 0.2, (c) 0.4 and (d) 0.7; the HAGBs, LAGBs and twins are indicated by thick-black, thin-white and thick-red lines, respectively.

When the strain is increased to 0.2, above the peak strain, a lot of DRX grains, essentially free of LAGBs, can be observed in the microstructure. Serrated or bulged boundaries are not observed anymore. However, there are still some un-recrystallized grains with relatively high density of LAGBs (see white boundaries in Fig. 5b-c).

As shown in Fig. 5d, with the further increase of strain to 0.7, the elongated grains disappear, finer and equiaxed grains are dominant and complete DRX occurs. However, there are still some grains containing low angle boundaries in their interior. These are work-hardened

dynamically recrystallized grains [27,51], in which new cycles of recrystallization occur, shown by green arrows in Fig. 5d.

Fig. 6 shows the influence of strain on the misorientation angle distribution of grain boundaries of samples compressed at 1100 °C and 0.1 s^{-1}. It is evident that the distribution of the misorientation angles shifts to the high angles with further increasing the strain. The average misorientation angles can be determined as 27.68, 36.18, 40.98 and 40.91, for the evaluated strains in an increasing order. As it is observed in Fig. 6b-d, there is a sharp rising of the fraction of grain boundaries having about 60° misorientation angle for samples deformed at high strains. This is related to the formation of twins during the hot deformation, shown as red lines in Fig. 5.

The point to point (local) and point to origin (cumulative) misorientations of two characteristic microstructures were plotted along the lines drawn in Fig. 7, to assess the impact of strain on the misorientation gradient. As observed in Fig. 7b and c, the local and cumulative misorientations do not exceed values of 2 and 4°, respectively, for the sample compressed to a strain of 0.05 at 1100 °C and 0.1 s^{-1}. However, when the strain is increased to 0.2, the misorientation along the line B1 exceeds 10° at a distance of 25 µm, as shown in Fig. 7e, and the scan data along the cross-section of the grain, Fig. 7f, shows that the cumulative misorientation exceeds 15°.

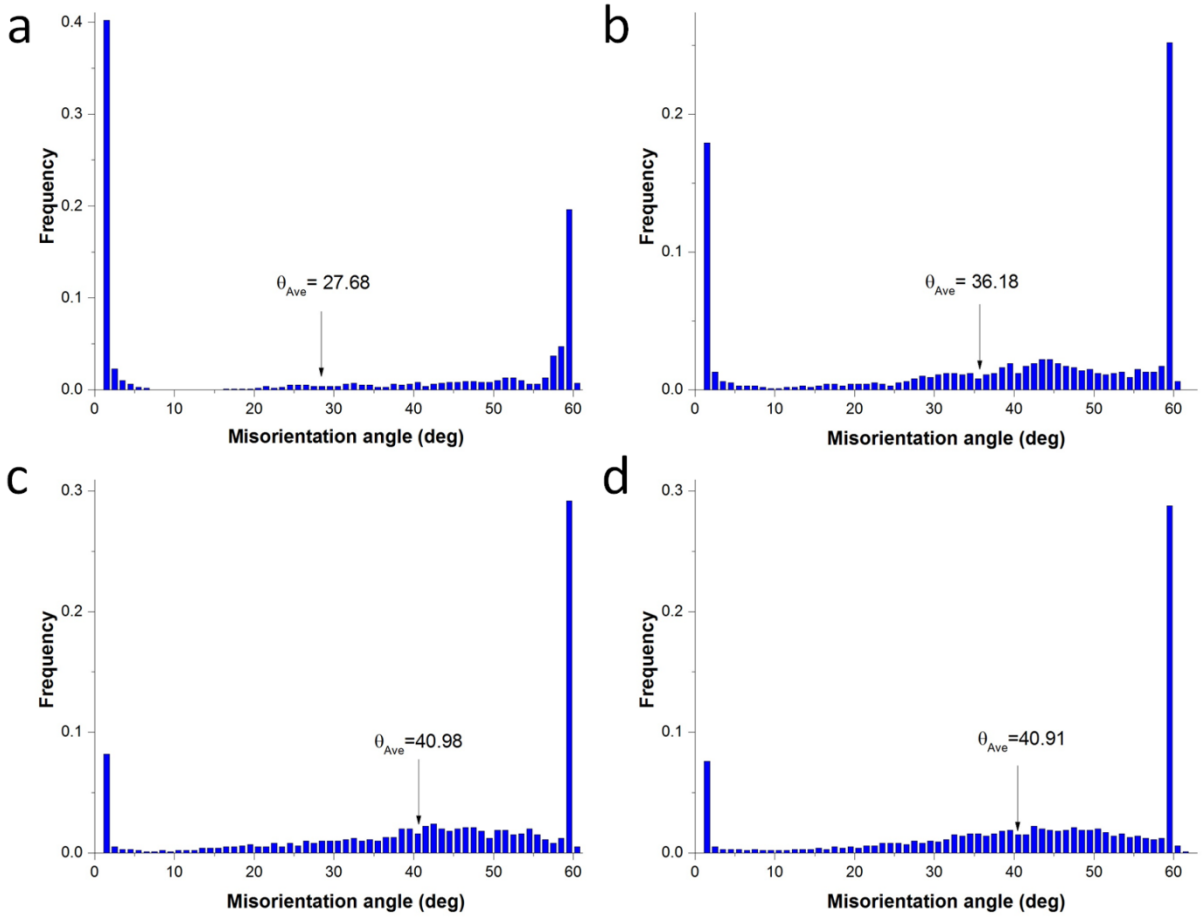

Fig. 6. Misorientation angle distributions of the deformed IN718 samples under 1100 °C and 0.1 s^{-1} at the strains of (a) 0.05, (b) 0.2, (c) 0.4 and (d) 0.7.

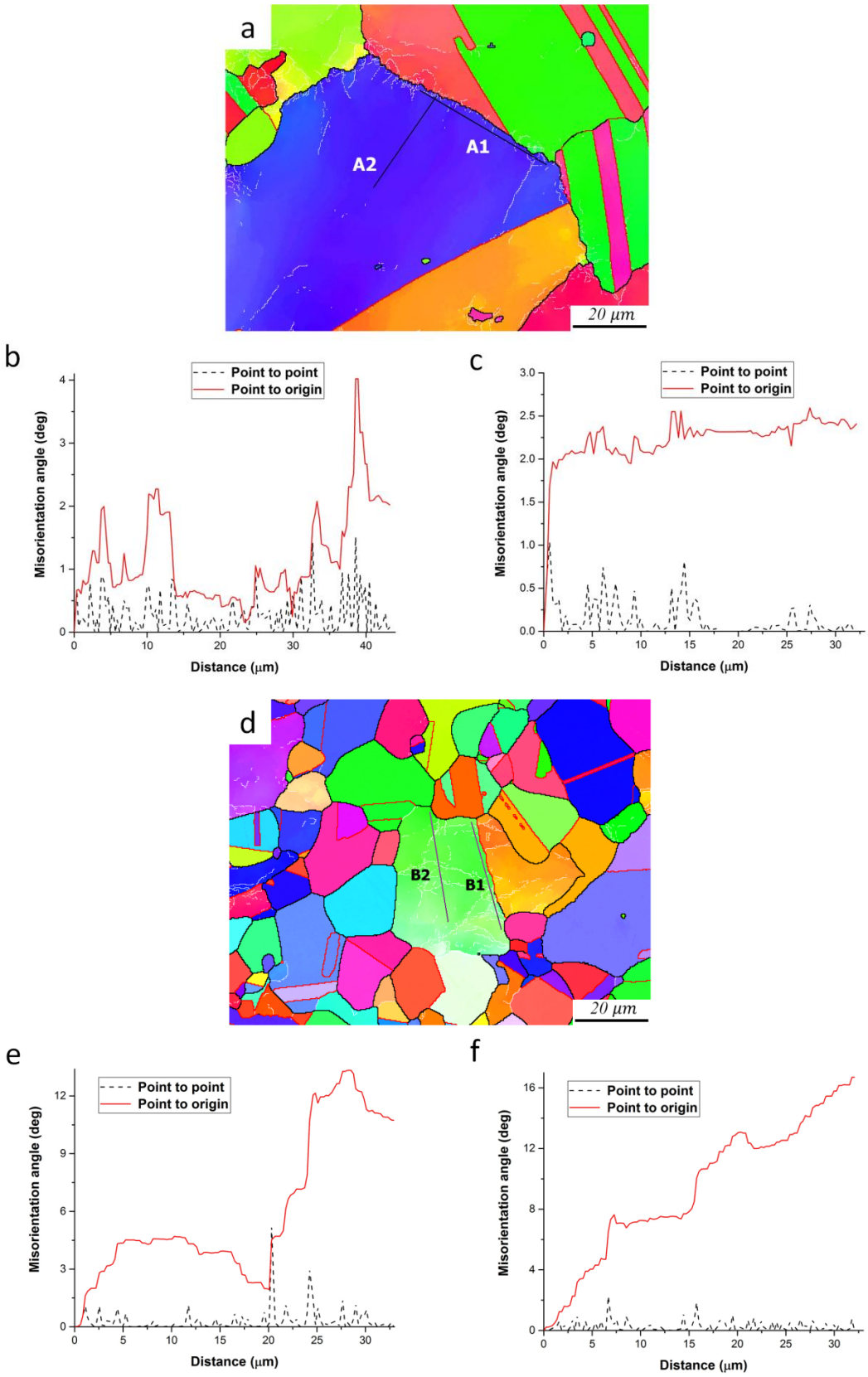

Fig. 7. OIM maps and orientation analysis of IN718 samples deformed at 1100 °C and strain rate of 0.1 s^{-1} to different strains. (a) typical OIM map at a strain of 0.05; (b) and (c) misorientations measured along the lines A1 and A2 marked in (a); (d) typical OIM map at a strain of 0.2; (e) and (f) misorientations measured along the lines B1 and B2 marked in (d).

3.3.2. Effect of the deformation temperature

Fig. 8a and b exhibit the orientation microscopy image maps of the samples hot compressed under a strain rate of 1 s^{-1} at two deformation temperatures (1000 and 1050 ºC) and a strain of 0.7. It is evident that most of the grains are elongated, and only a few recrystallized grains are visible at the original grain boundaries in the sample deformed at 1000 °C and 1 s^{-1}. The deformed microstructure is inhomogeneous and band structures are obvious in some deformed grains, shown by arrows in Fig. 8a. As shown in Fig. 8a and b, the fraction of DRX grains increases with increasing the deformation temperature from 1000 to 1050 °C. This can be ascribed to the lower critical dislocation density for the occurrence of DRX at higher temperatures [43]. It is interesting to note that almost none of the observed recrystallized grains are present in the interior of the initial grains. It can be observed that due to the concurrent deformation, the twins inside the elongated grains lose their specific twin orientation. However, recrystallized grains are strongly twinned specially at higher temperatures, and a large fraction of grain boundaries formed after DRX initiation has Σ3 twin relationship.

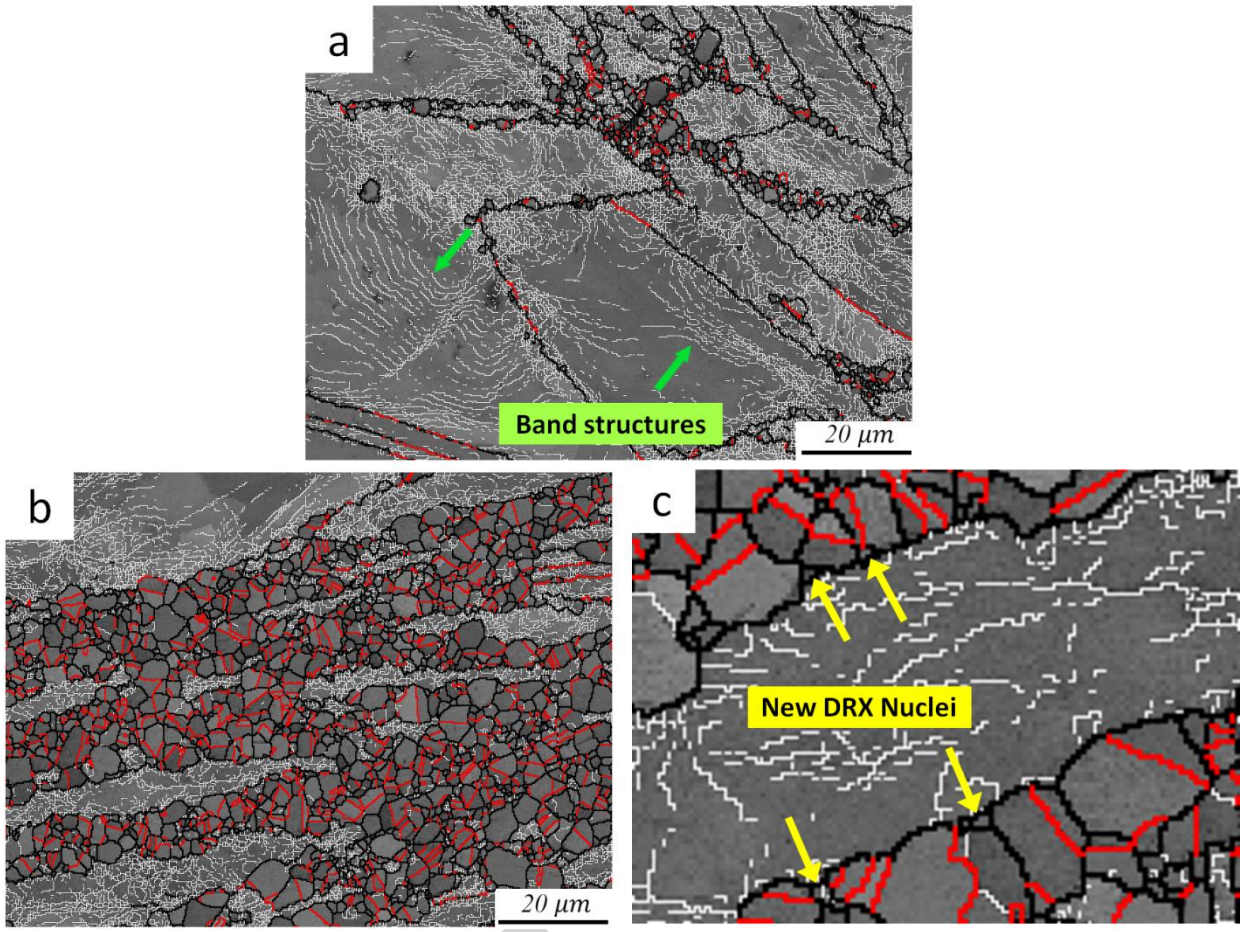

Fig. 8. OIM maps of IN718 samples deformed at strain rate of 1 s^{-1} and temperatures of (a) 1000, (b) 1050 °C and (c) a magnified region of (b); the HAGBs, LAGBs and twins are indicated by thick-black, thin-white and thick-red lines, respectively.

The relative frequency changes of the misorientation angle at different deformation temperatures for the sample deformed at strain rate of 1 s^{-1} are summarized in Fig. 9. As illustrated in Fig. 10a, the fraction of LAGBs is predominant at lower temperatures. With raising the deformation temperature, the fraction of HAGBs is increased.

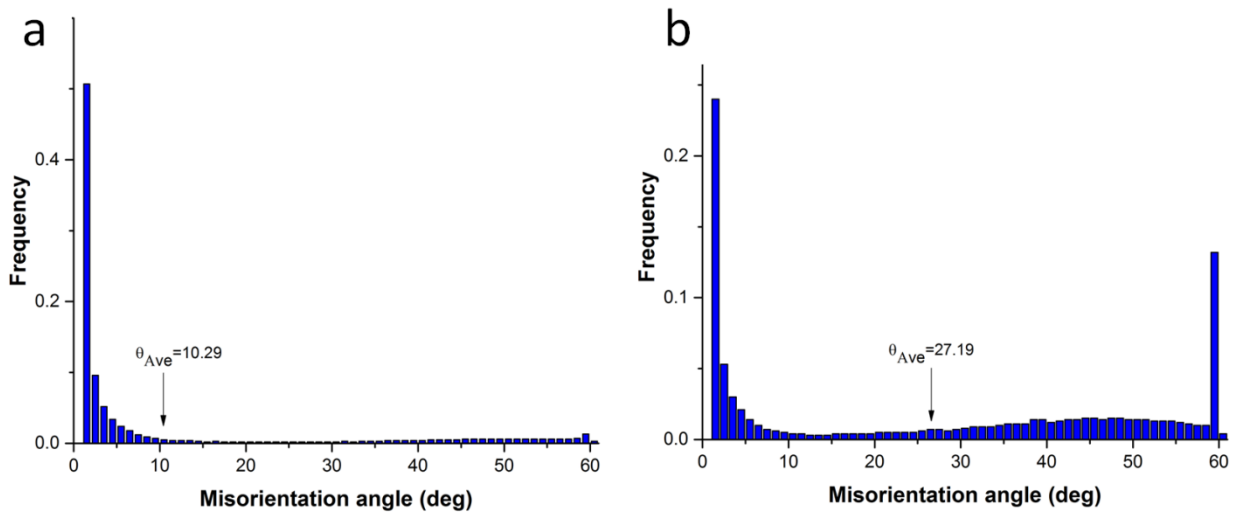

Fig. 9. Misorientation angle distributions of the deformed IN718 samples under strain rate of 1 s^{-1} and temperatures of (a) 1000 and (b) 1050 °C, at a strain of 0.7.

To clarify the influence of deformation temperature on the DRX mechanisms, the misorientation analysis was performed along the lines shown in Fig. 10a and d. The cumulative misorientations developed along the C1 and C2 line exhibit a large orientation gradient along the grain boundary as well as within the grain. It is apparent from Fig. 10b that the local misorientation does not exceed 6°, while the cumulative misorientation continuously increases to 32° (at a distance of 20μm). With increasing deformation temperature, the cumulative misorientations decrease significantly, as displayed in Fig. 10e and f.

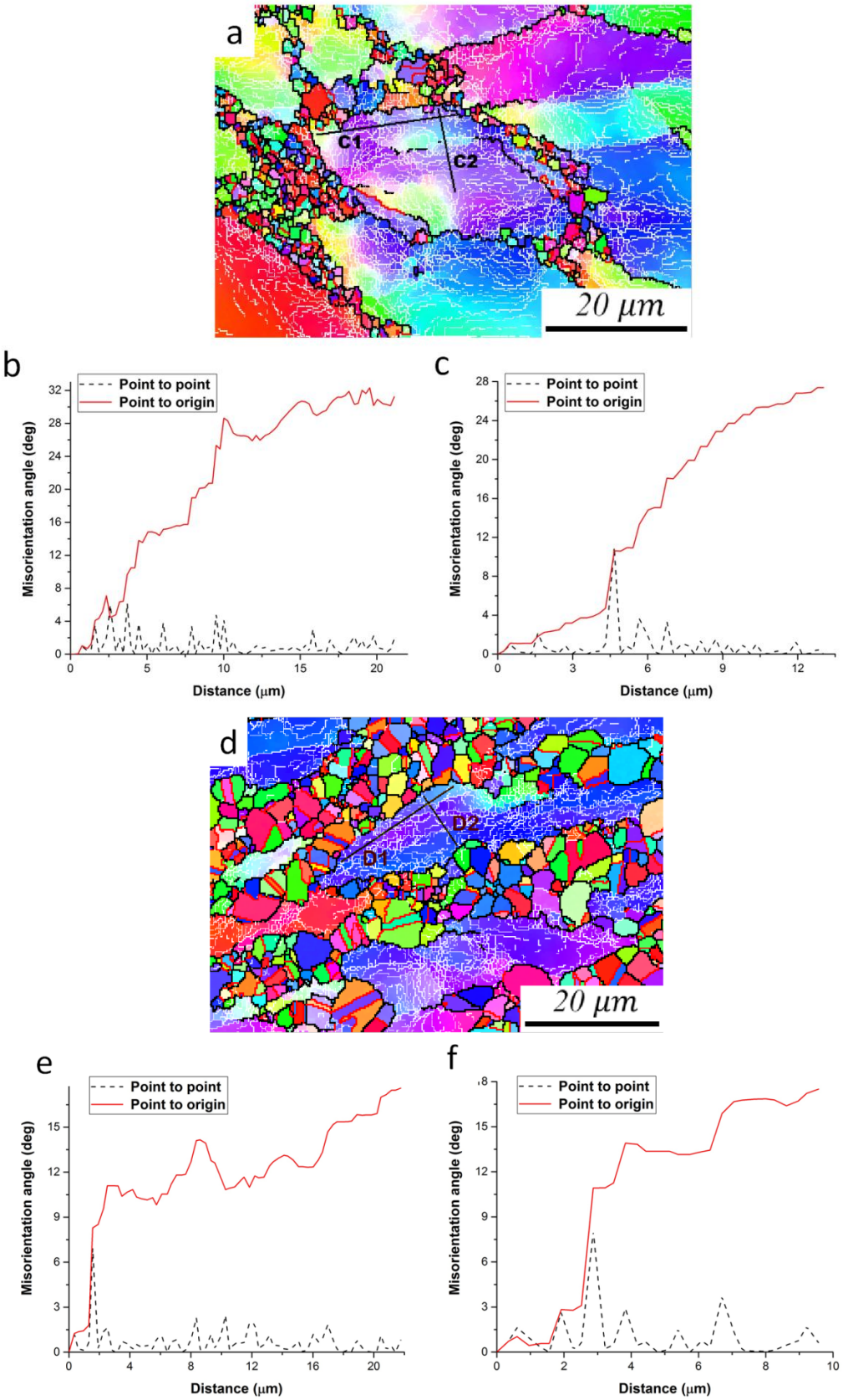

Fig. 10. OIM maps and orientation analysis of the IN718 samples deformed at strain rate of 1 s^{-1} and different temperatures to a strain of 0.7. (a) typical OIM map at 1000 °C ; (b) and (c) misorientations measured along the lines C1 and C2 marked in (a); (d) typical OIM map at 1050 °C; (e) and (f) misorientations measured along the lines D1 and D2 marked in (d).

3.3.3. Effect of strain rate

The effects of strain rate on the subgrain structures obtained at 950 °C after applying a strain of 0.7 are depicted in Fig. 11. DRX grains free of LAGBs can be found in both microstructures deformed under strain rates of 0.001 and 0.01 s^{-1}, however, the fraction and size of these grains decrease with increasing strain rate. Results show that almost all the recrystallized grains of small size have no annealing twins, shown by green arrows in Fig. 11, while most of the larger grains contain twins, especially in the samples deformed at lower strain rates.

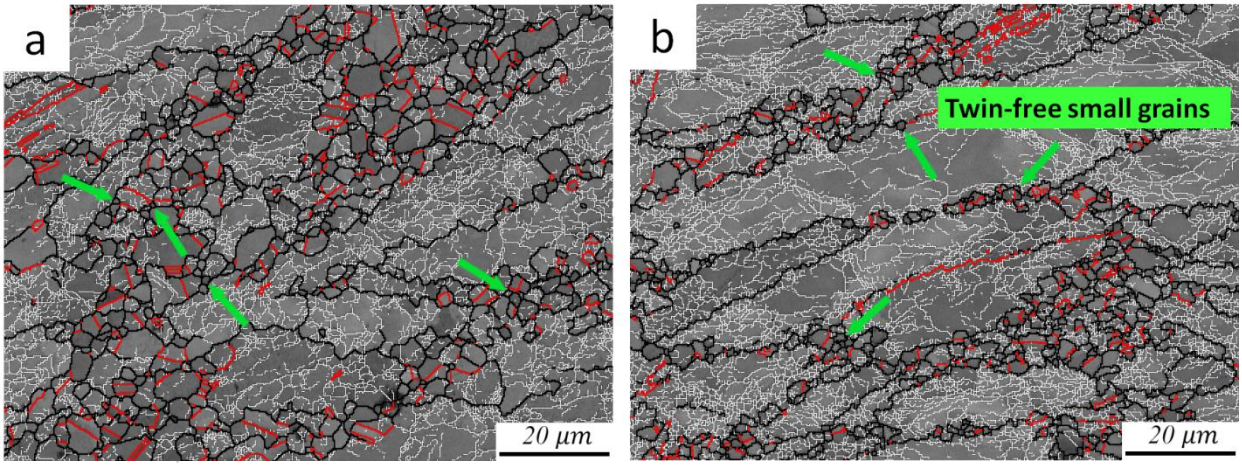

Fig. 11. OIM maps of samples deformed at temperature of 950 °C and strain rates of (a) 0.001 and (b) 0.01 s^{-1}; the HAGBs, LABs and twins are indicated by thick-black, thin-white and thick-red lines, respectively.

The fractions of grain boundaries with different misorientation angles, for the IN718 sample deformed at 950 °C, as a function of strain rate are plotted in Fig. 12. It can be observed

that the fraction of LAGBs increases with raising the strain rate, and the average misorientation angles falls from 19.25 to 13.58°. Moreover, the fraction of medium angle boundaries (MAGBs) with misorientation of 10–15° increases as strain rate increases. It appears from Fig. 13 that both the cumulative misorientation and local misorientation along grain boundary and grain interior, observed at high strain rates are remarkably higher than those at low strain rates. Likewise, the misorientation of geometrically necessary boundaries (GNBs) obtained at the strain rate of 0.001 s^{-1} is 4° (Fig. 13b and c), whereas the misorientation at the strain rate of 0.01 s^{-1} is greater than 10° (Fig. 13e and f).

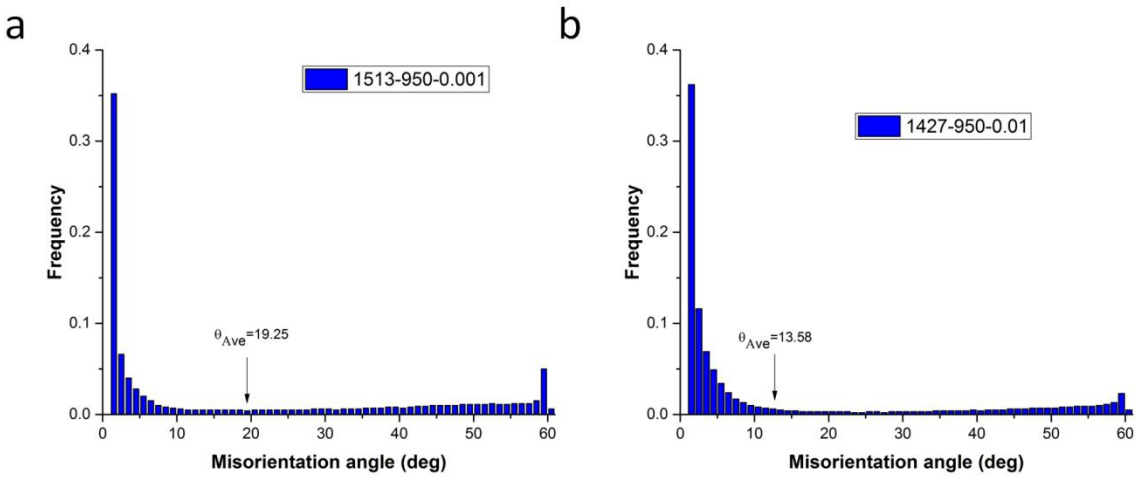

Fig. 12. Misorientation angle distributions of the deformed IN718 samples at temperature of 950 °C and strain rates of (a) 0.001 and (b) 0.01 s^{-1}, to a strain of 0.7.

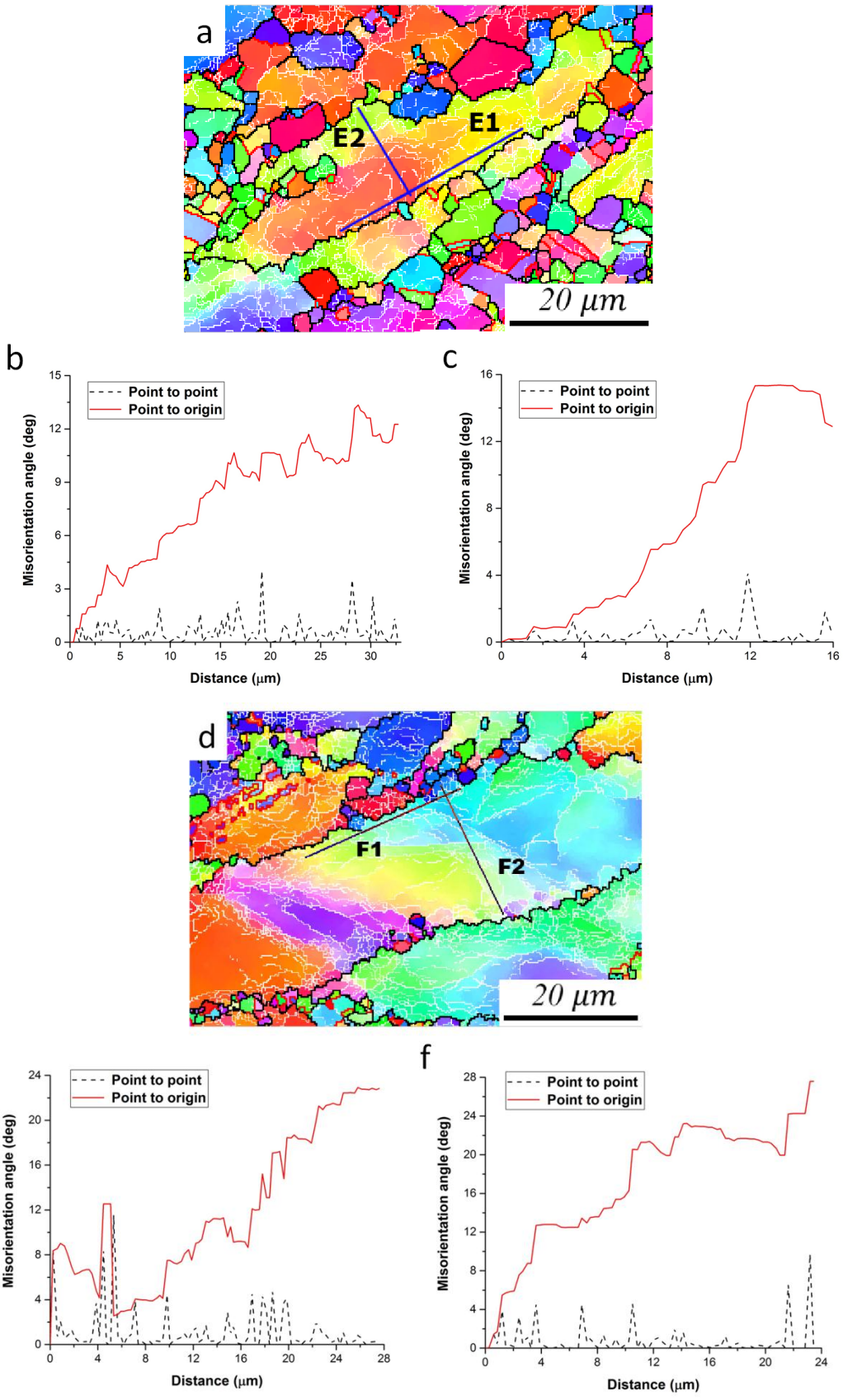
a
E1
E2
20 μm
b
Point to point
Point to origin
Misorientation angle (deg)
Distance (μm)
c
Point to point
Point to origin
Misorientation angle (deg)
Distance (μm)
d
F1
F2
20 μm
e
Point to point
Point to origin
Misorientation angle (deg)
Distance (μm)
f
Point to point
Point to origin
Misorientation angle (deg)
Distance (μm)

Fig. 13. OIM maps and orientation analysis of the IN718 samples deformed at 950 °C and different strain rates and strain of 0.7. (a) typical OIM map at a strain rate of 0.001 s^{-1}; (b) and (c) misorientations measured along the lines E1 and E2 marked in (a); (d) typical OIM map at strain rate of 0.01 s^{-1}; (e) and (f) misorientations measured along the lines F1 and F2 marked in (d).

4. Discussion

4.1. Recrystallization mechanisms

4.1.1. The role of deformation parameters

Generally, DDRX, also known as conventional DRX, takes place in cubic metals with low or medium stacking fault energy [52,53], and it features nucleation by grain boundary bulging followed by growth of the recrystallized grains [54,55]. However, grain boundary bulging needs developing subgrains near the pre-existing grain boundaries in order to provide the driving force required for local migration of the grain boundary [56]. On the contrary, CDRX takes place by generation of low angle grain boundaries (LAGBs), which transform to high angle grain boundaries (HAGBs) with further deformation. Therefore, CDRX is substantially related to the formation of subgrains or LAGBs, and the new grains do not appear by a nucleation and growth process, as in DDRX [57]. The magnitude of strain has a strong effect on the softening behavior of the studied IN718. It can be found from Fig. 5 that under relatively small strains the grain boundaries are highly serrated. These serrated regions are potential sites for the subsequent nucleation through the grain boundary bulging [36]. This indicates that DDRX, featured by grain boundary bulging, is the primary nucleation mechanism of DRX for the IN718 samples during the hot compression at 1100 ºC and small strains. Generally, grain boundary bulging is driven by

the energy difference between the adjacent grains, and is indicative of strain-induced grain-boundary migration (SIGBM) [58].

Considering Fig. 5, bulged boundaries are vanished and the amount of subgrains in the interior parts of the un-recrystallized grains is increased with further increasing the strain. This fact suggests that CDRX is starting to be an active DRX mechanism. CDRX is typically characterized by progressive subgrain rotation, which induces the generation of LAGBs, the subsequent increase of the misorientation angles and their possible transformation into HAGBs. Furthermore, incomplete discontinuous HAGB segments are frequently observed within grains in the EBSD maps, which are connected by LAGBs, as shown by white arrows in Fig. 5b-c. Accordingly, it can be concluded that these kind of discontinuous HAGBs have evolved from the LAGBs by continuous absorption of dislocations (CDRX) [59]. The fraction of LAGBs (f_{LAGB}) at the strains of 0.05, 0.2, 0.4 and 0.7 were determined as 0.45, 0.23, 0.11 and 0.11, respectively, for specimens deformed at 1100 °C and 0.1 s^{-1}, shown in Fig. 14a. The stored energy is not sufficient for the onset of DRX and transition from low angle to high angle boundaries at small strains. As OIM images showed (Fig. 5a), most of the LAGBs are concentrated onto old grain boundaries, and there are no dislocation cells in the structure. This implies that dynamic recovery is not discernible and the fraction of LAGBs is relatively high. At this stage, DRX would be of the DDRX type. On the other hand, both the local and cumulative misorientations along the original HAGBs or from the grain boundary to the grain interior do not exceed 4°, shown in Fig. 7b and c. Thus, it can be concluded that at small strains most of the subgrain boundaries are still under development and CDRX cannot take place. As DRX progresses at larger strains, the strain-free grains lead to the gradual diminution of dislocations and the fraction of LAGBs decreases.

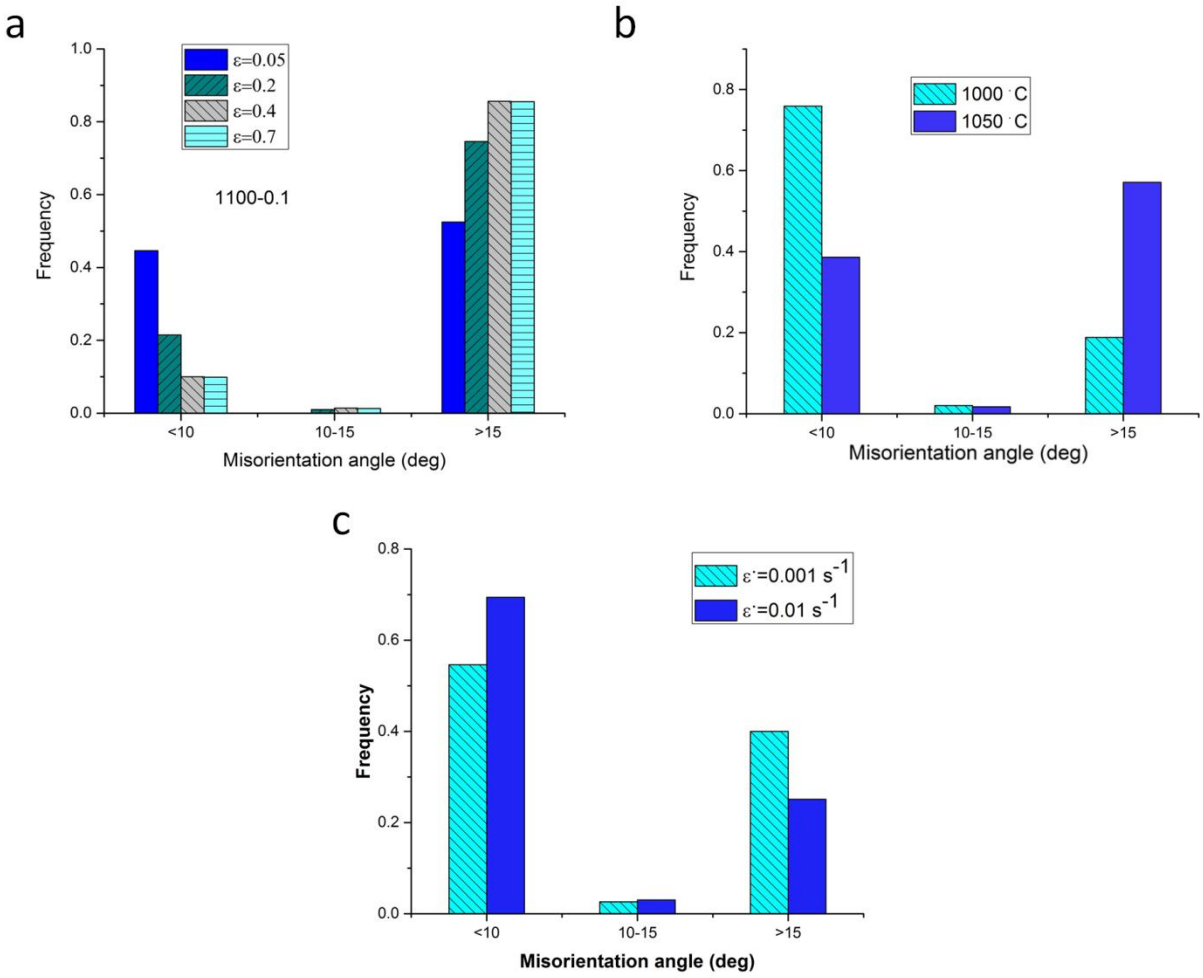

Fig. 14. Misorientation angle distributions of the deformed IN718 samples under (a) temperature of 1100 °C and strain rate of 0.1 s^{-1} at the various strains, (b) strain rate of 1 s^{-1} and various temperatures, and (c) temperature of 950 °C and various strain rates.

The development of the CDRX is characterized by progressive subgrain rotation and a misorientation angle between 10 and 15°, MAGBs , which is required for nucleation of recrystallized grains through this mechanism [24]. The point to the origin misorientation exceeded 10° along original grain boundaries as is shown in Fig. 7e. Thus, the medium to high angle dislocation boundaries generated near the original grain boundaries. This indicates the stronger effect of continuous progressive subgrain rotation and thereby CDRX at higher strains.

Deformation temperature has a significant influence on the size, fraction and recrystallization mechanism of DRX grains. A large fraction of big recrystallized grains is observed at high temperatures, shown in Fig. 8. This is owing to the effects of the thermally activated phenomena during the recrystallization. The recrystallized grains grew more easily and became coarser because dislocation mobility accelerated and diffusion rate increased at high temperatures, which is in line with the findings of Shahri et al. [60].

It is clear from Fig. 14b that the fraction of HAGBs is increased with increasing the temperature. This is due to the development of dislocation-free recrystallized grains, which is in agreement with Fig. 8b and c, and investigations of Jiang [37]. MAGBs decrease slightly with increasing the deformation temperature, which proves the weak effect of progressive subgrain rotation at the high deformation temperature. This finding is in good agreement with the observations in Fig. 10. Fig. 10 shows the relationship between cumulative misorientations and temperature and indicates that the effects of CDRX become weaker at higher temperatures. However, some features of CDRX such as subgrains with LAGBs and individual HAGBs in the interiors of the original grains can be observed in Fig. 8b.

Fig. 10e-f shows that at low deformation temperatures, the cumulative misorientations display a large orientation gradient along both the grain boundary and within the grain. This implies that the mechanism of CDRX has a significant role in the DRX process at low deformation temperature. Unlike the cumulative misorientations, the local misorientations show a small orientation gradient which indicates that the GNBs formed in the deformed grains. GNBs are considered to accommodate the mismatch in the lattice rotation induced by regions of different slip on either side [61]. The various local crystallographic orientations in a grain caused by strain incompabilities between neighboring deformed grains generate GNBs. Besides,

individual boundaries with high misorientations in the original grain interiors (Fig. 10c) are related to the development of GNBs or deformation bands.

Strain rate is another key parameter affecting the recrystallization mechanism. The critical strain for recrystallization increases with increasing the strain rate [62]. A large amount of dislocations is provided for the formation of DRX nuclei at high strain rate, but dislocation rearrengment and annihilatioin for the formation of nuclei of DRX grains is restricted. This is the reason why increasing the strain rate results in decreasing the fraction and size of the recrystallized grains. Fig. 14c shows that both LAGBs and MAGBs fractions increase with raising the strain rate. This implies that the CDRX mechanism based on the continuous subgrain rotation is promoted at high strain rates. Moreover, a higher cumulative and local misorientation along both the grain boundaries and grain interiors, illustrated in Fig. 13, indicates that the occurrence of CDRX, which is closely related to the dislocation density [38], is more likely to occur at high strain rates. Grains division into parts with different orientation bands is a result of CDRX operating at high strain rates. Fig. 13e shows that three main misorientation jumps are located at about 0.5, 4, 5 and 15 μm from the origin, which implies a misorientation of about 8–12°.

High cumulative and local misorientation along the grain boundary and grain interior at high strain rates (Fig. 13e and f) indicates that deformation is heterogeneously distributed and particularly localized in the vicinities of the grain boundaries. Heterogeneous strain will result in a significant serration of the grain boundaries [63]. This is in conformity with the OIM image presented in Fig. 11.b, which shows intensely serrated grain boundaries. Regions with high localized strain can connect with each other and result in the development of micro-shear zones, as reported in the previous work of the authors [43].

4.1.2. The preferred sites for nucleation

Fig. 11 depicts the typical features of DDRX, in which the grain boundaries are extensively serrated and bulged, with plenty of DRX grains consisting of HAGBs. The grains along the prior grain boundaries with a necklace structure are a result of DDRX mechanism. Following the formation of the first layer of DRX grains at the pre−existing grain boundaries, next layers form at the interface of the original grains and DRX grains of the first layer, shown in Fig. 8b and c. It appears that the nucleation sites for new DRX grains are triple junctions, as indicated by the arrows in Fig. 8c. Triple junctions have excess energy beyond the energy of neighboring boundaries [64], and dislocation density at or near triple junctions are significantly higher than at neighboring grain boundaries [65]. Therefore, these places are preferred sites for the nucleation of DRX grains. Moreover, boundaries of pre-existing grains are concave in the triple junctions, but neighboring boundaries show convex surfaces. Consequently, nucleated grains in the triple junctions have a low surface area to volume ratio and, thus, a low surface energy per unit volume. Convex portions of the primary boundaries, which cause concavity in the triple junctions, are the consequence of the growth mechanism of the DRX layers produced the preceding stage. If the amount of discontinuous precipitations is small, the main forces acting on the recrystallization front are provided by deformation and grain boundaries [66]. The latter is related to the grain growth and secondary recrystallization mechanisms, where the total amount of grain boundaries tends to be minimized. Although the driving force for growth of DRX nuclei is supplied by deformation, it seems that the shape of DRX grains is controlled by grain surface energy and surrounding grains. This is the reason why almost all DRX grains have equiaxed morphology.

4.2. Twinning evaluation

4.2.1. The role of twins in recrystallization

Ni-based superalloys with low stacking fault energy display a huge propensity for twinning during DRX. It is well known that the formation of twins decreases the boundary energy of growing grains [36]. Hence, it is predicted that DRX process progresses by promoting grain boundaries with twin orientation. Fig. 11 depicts that almost all small DRX grains are free of twins, while most of the larger grains contain twins. Thus, it can be inferred that twins generate during the growth of the recrystallized grains. These twins can be regarded as annealing twins owing to the similarities in the grain boundary types and absence of plastic deformation in the recrystallized structure.

Primary twins Σ3, characterized by 60° misorientation around ⟨111⟩, and higher order twins, including Σ9 (38.9° / ⟨101⟩)[67], Σ27a (31.6° /⟨110⟩) [68] and Σ27b (35.4° /⟨210⟩) [69], were considered. From CSL rule [70], interaction between Σ3 boundaries can form a Σ9 boundary according to the relationship Σ3 + Σ3 = Σ9, marked by yellow arrows in Fig. 15. When a Σ9 boundary meets another Σ3 boundary, it generates either a new Σ3 boundary (Σ3 + Σ9 = Σ3), or a Σ27 boundary (Σ3 + Σ9 = Σ27). As many twins are formed within a grain, adjacent twins can encounter each other and form higher order twins at the triple junctions. The generated Σ3, Σ9 and Σ27 boundaries can be observed in Fig. 15, in which the OIM maps of the alloy deformed to the 0.7 true strain and various temperatures and strain rates are shown. In Fig. 15, Σ3, Σ9 and Σ27 boundaries are shown by red, yellow and green lines, respectively. It is obvious that the deformation has a discernible effect on the twin boundary characteristics. Most of the twin boundaries pre-existing in the matrix lose their coherency characteristics (angle/axis), and

convert to the general high-angle boundaries during the hot compression (marked by green arrows in Fig. 15).

As indicated in Fig. 15, a great number of twins form inside the recrystallized grains, behind the migrating grain boundaries. One of them is displayed in the circle A in Fig. 15b. Multiple twinning is also present within the recrystallized grains, marked by circle B in Fig 15b. Wang et al. have proposed that the driving force for twin formation near the triple junctions of moving grain boundaries is the decline in the interfacial energy [71]. This is the reason why twinning is considered a stacking error [72] or a 'growth accident' [40], taking place at the grain boundaries or triple junctions.

It has been shown in Ref. [71] that the normal direction of the coherent twin planes is usually close to the growth direction of grains. The growth direction of a DRX grain can be deduced from the curvature of the migrating boundaries. The dependency of coherent twins to the growth direction can be observed in Fig. 15 a-b, in which blue arrows show the growth direction of the recrystallized grains. This can explain the formation of the parallel twins in some recrystallized grains.

The effects of deformation temperature and strain rate on the twin formation in the present IN718 are illustrated in Fig. 15c-d and e-f, respectively. It is evident that higher temperatures and lower strain rates facilitate the formation of the twin boundaries. This finding can be ascribed to the fact that with increasing the deformation temperature and decreasing strain rate the growth step of recrystallized grains is promoted.

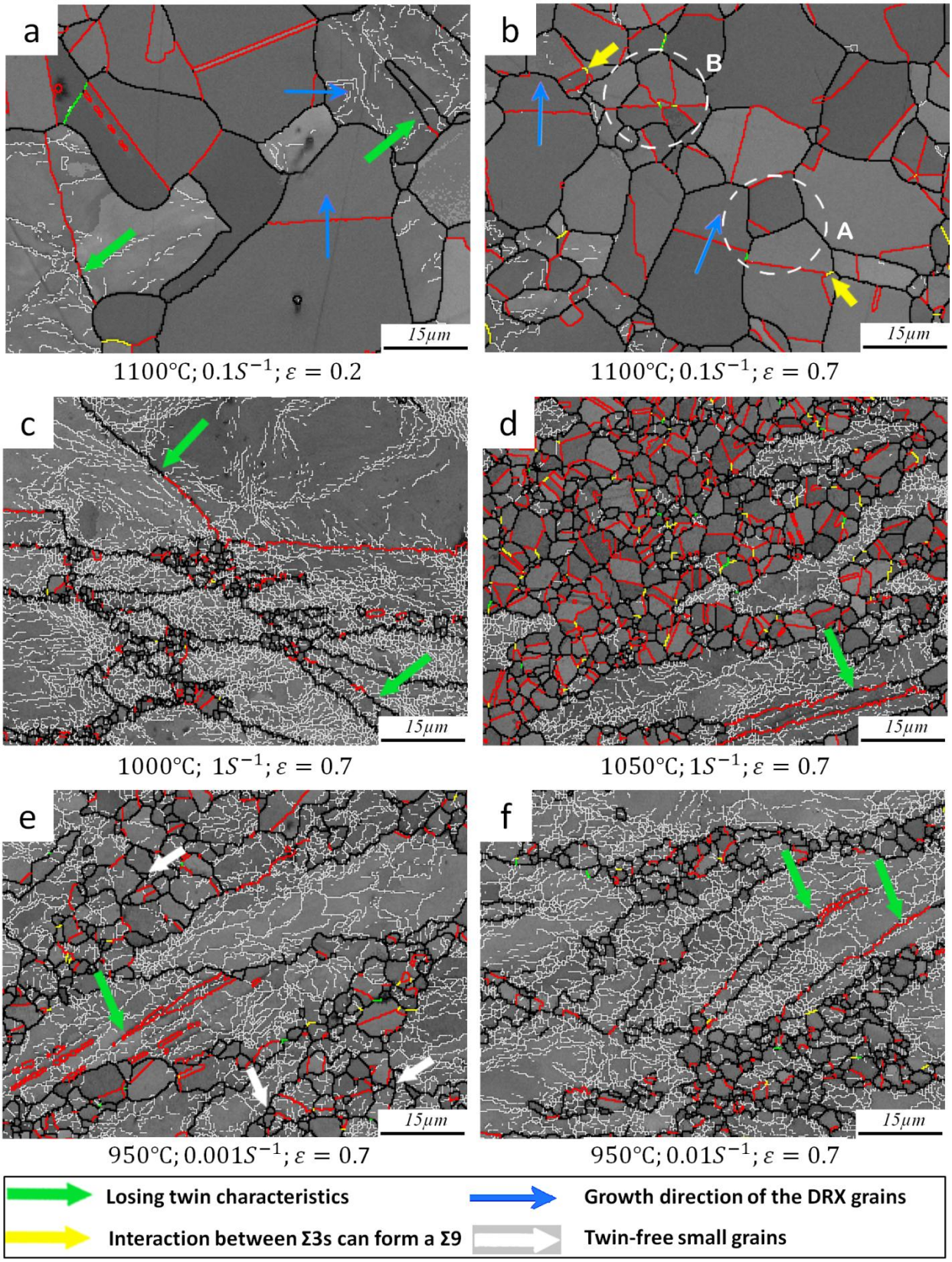
a
15μm
1100°C; 0.1S^{-1}; $\varepsilon = 0.2$
b
B
A
15μm
1100°C; 0.1S^{-1}; $\varepsilon = 0.7$
c
15μm
1000°C; 1S^{-1}; $\varepsilon = 0.7$
d
15μm
1050°C; 1S^{-1}; $\varepsilon = 0.7$
e
15μm
950°C; 0.001S^{-1}; $\varepsilon = 0.7$
f
15μm
950°C; 0.01S^{-1}; $\varepsilon = 0.7$
Losing twin characteristics
Growth direction of the DRX grains
Interaction between Σ3s can form a Σ9
Twin-free small grains

Fig. 15. OIM maps of IN718 samples deformed at different conditions. The HAGBs, LABs and Σ3 twins are indicated by thick-black, thin-white and thick-red lines, respectively. Also, Σ9 and Σ27 twins are displayed by yellow and green lines, respectively.

It is interesting to note that DRX grains can form on both sides of the bulged grain boundaries (Fig. 16a). Nucleation of DRX grains through the formation of the annealing twins on the bulging boundaries shows the important role of the twinning in the DDRX mechanism. A step by step schematic illustration of this process is depicted in Fig. 16b for the sample deformed at 1100 °C and strain rate of 0.1 s^{-1} to a strain of 0.05. The process can be described as follows. (I) In the first stage of deformation, the primary grain boundaries are serrated; (II) then, grain boundary bulging occurs; (III) new recrystallized grains are nucleated by twining behind the bulged areas; (IV-V) parts of ∑3 boundaries lose their twin characteristic during growth of nuclei; (VI) it is anticipated that in the next steps of the deformation, all parts of the growing boundaries lose their ∑3 characteristics. A constitutive characteristic of DDRX can be found in (IV-V) stages of Fig. 16b which shows a large-scale boundary growth. It is believed that discontinuously recrystallized grains form by nucleation occurring at highly strained regions followed by a large-scale grain boundary migration; in other words, DDRX can be considered as a two-step process. However, continuously recrystallized grains are in fact strain-induced ultra fine grains with a small-scale grain boundary migration; so, it is a one-step process.

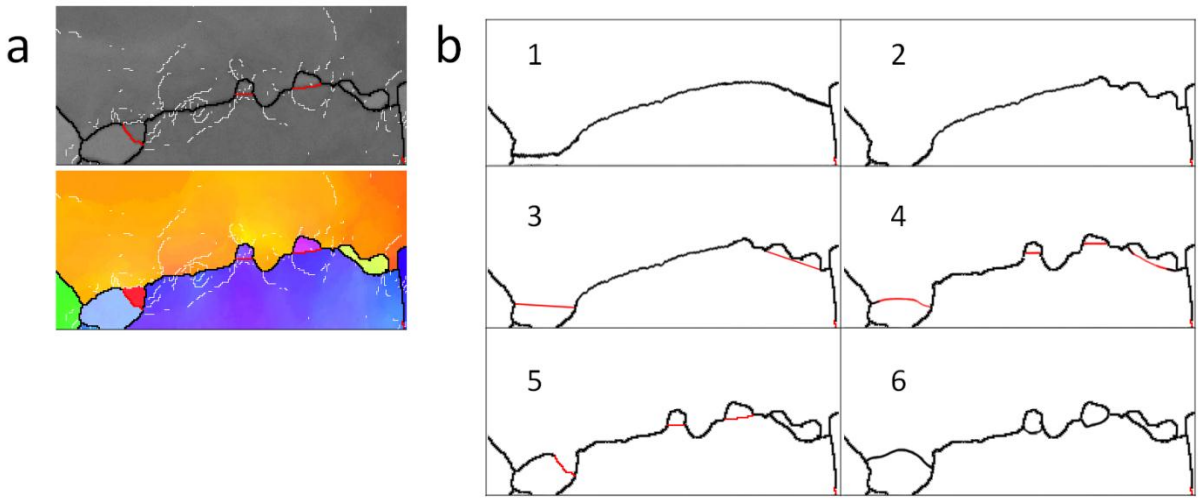

Fig. 16. (a) OIM maps and (b) schematic illustrations of the dynamic nucleation at matrix boundaries in the IN718 sample during deformation at 1100 °C and 0.1 s^{-1} up to a strain of 0.05.

Taking into account the details of Figs. 15-16, it can be concluded that interior regions of the recrystallized grains, nucleated behind the bulged pre-existing boundaries, are free of twins (small grains marked by white arrows in Fig. 15 and nucleated grains in Fig. 16a). On the other hand, most of the grown DRX grains contain twins and multiple twins. Hence, it is suggested that twins inside the DRX grains are mostly formed during the growth stage, which is in good agreement with the results obtained by Beladi et.al [73].

4.2.2. Interaction of twins and secondary phases

The main difference between an ordinary HAGB and a coherent twin boundary is illustrated in Fig. 17 in which an OIM image of the initial structure of IN718 sample and schematics of these boundaries are shown. Both A1 and A2 marked grain boundaries in Fig. 17a have intersections with secondary phase particles (carbides or nitrides). A1 grain boundary is an ordinary HAGB while A2 grain boundaries are twin boundaries. It can be observed that in the case of the ordinary HAGB (A1), the particles exert a restraining force upon the boundary and

pull back the boundary at the particle location, but there is no pulling back for twin boundaries (A2). It means that restraining force acting on an ordinary HAGB is greater in comparison with the force applied on a twin boundary. The amount of this force determines the angle between "grain boundaries" and "tangent to the particle", see angle α in Fig. 17b. This is why the resulted angle α for a twin boundary is 90° which is more than that of an ordinary HAGB. This behavior can be attributed to the difference between the surface energy of an ordinary HAGB and a coherent twin boundary. According to Zener theory, if the boundary meets a particle, then the restraining force on the boundary is directly proportional to the surface energy of the boundary [74,75]. A coherent twin boundary has almost complete atomic fit across the interface that results in low energy. It has been reported that the coherent twin boundary energy is 0.03 J/m^2 while an ordinary HAGB energy is 0.69 J/m^2 in nickel [76]. Therefore, an ordinary HAGB with high energy is under a high restraining force.

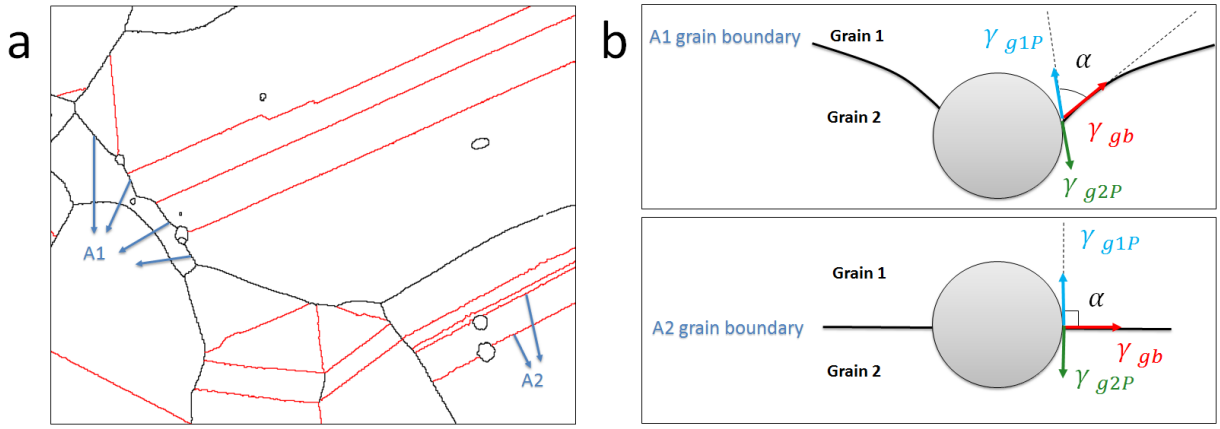

Fig. 17. (a) OIM map and (b) schematic illustrations showing the interaction of secondary phase particles with an ordinary HAGB and twin boundaries in the initial microstructure of the studied IN718.

Conclusions

The microstructural evolution of IN718 was studied by hot compression tests. The effects of deformation parameters on the microstructural evolution were analyzed. The following conclusions can be made.

-The DDRX mechanism is the major deformation mechanism at low strains for the studied IN718. However, CDRX mechanism is promoted with increasing strain.

-Fraction of LAGBs, cumulative and local misorientations along the grain boundary and grain interior as well as misorientation of GNBs increases with raising the strain rate and decreasing deformation temperatures, indicating that the CDRX mechanism is promoted.

-Twins formation is facilitated at higher temperatures and lower strain rates.

-Following DRX nucleation by twining behind the bulged areas, nuclei lose their ∑3 characteristic during growth. However, twins will generate again inside the DRX grains during the growth of grains.

Acknowledgements

The authors would like to thank Fundacióo´ CTM Centre Tecnologic (Manresa, Spain) for providing the facilities for the experimental works. The authors also thank Dr. A. Gironés Molera, A. Hernandez and J. A. Muñoz Bolaños for their assistance in the experiments.

References

[1] K. Kulawik, P.A. Buffat, A. Kruk, A.M. Wusatowska-Sarnek, A. Czyrska-Filemonowicz, Imaging and characterization of γ′ and γ″ nanoparticles in Inconel 718 by EDX elemental mapping and FIB–SEM tomography, Mater. Charact. 100 (2015) 74–80.

[2] S. Khaja, K.K. Mehta, R.V. Babu, R.S.R. Devi, A.K. Singh, Mechanical Properties

Anisotropy of Isothermally Forged and Precipitation Hardened Inconel 718 Disk, Metall. Mater. Trans. A. 46 (2015) 1140–1153.

[3] F.-L. Sui, L.-X. Xu, L.-Q. Chen, X.-H. Liu, Processing map for hot working of Inconel 718 alloy, J. Mater. Process. Technol. 211 (2011) 433–440.

[4] M.C. Rezende, L.S. Araújo, S.B. Gabriel, J. Dille, L.H. de Almeida, Oxidation assisted intergranular cracking under loading at dynamic strain aging temperatures in Inconel 718 Superalloy, J. Alloys Compd. (2015).

[5] L.S. Araujo, D.S. dos Santos, S. Godet, J. Dille, A.L. Pinto, L.H. de Almeida, Analysis of Grain Boundary Character in a Fine-Grained Nickel-Based Superalloy 718, J. Mater. Eng. Perform. 23 (2014) 4130–4135.

[6] D. Zhang, W. Niu, X. Cao, Z. Liu, Effect of standard heat treatment on the microstructure and mechanical properties of selective laser melting manufactured Inconel 718 superalloy, Mater. Sci. Eng. A. (2015).

[7] W. Zheng, Z. Song, T. Lei, Q. Yong, Q. Xie, Static recrystallization behavior of Inconel 718 alloy during thermal deformation, J. Wuhan Univ. Technol. Sci. Ed. 29 (2014) 379–383.

[8] S.K. Iyer, C.J. Lissenden, Multiaxial constitutive model accounting for the strength-differential in Inconel 718, Int. J. Plast. 19 (2003) 2055–2081.

[9] S. Kumar, G.S. Rao, K. Chattopadhyay, G.S. Mahobia, N.C.S. Srinivas, V. Singh, Effect of surface nanostructure on tensile behavior of superalloy IN718, Mater. Des. 62 (2014) 76–82.

[10] J. Kundin, L. Mushongera, H. Emmerich, Phase-field modeling of microstructure formation during rapid solidification in Inconel 718 superalloy, Acta Mater. 95 (2015) 343–356.

[11] K. Prasad, R. Sarkar, P. Ghosal, V. Kumar, Tensile deformation behaviour of forged disc of IN 718 superalloy at 650° C, Mater. Des. 31 (2010) 4502–4507.

[12] A.S. Gill, A. Telang, V.K. Vasudevan, Characteristics of Surface Layers Formed on Inconel 718 by Laser Shock Peening With and Without a Protective Coating, J. Mater. Process. Technol. (2015).

[13] K.G. Thirugnanasambantham, S. Natarajan, Degradation Through Erosion: Mechanistic Studies on IN-718 Superalloy Under Hot Air Jet Conditions, J. Mater. Eng. Perform. (n.d.) 1–9.

[14] K.C.G. Candioto, F.R. Caliari, D.A.P. Reis, A.A. Couto, C.A. Nunes, Characterization of the Superalloy Inconel 718 After Double Aging Heat Treatment, in: Mech. Mater. Eng. Mod. Struct. Compon. Des., Springer, 2015: pp. 293–300.

[15] Y. Wang, W.Z. Shao, L. Zhen, C. Yang, X.M. Zhang, Tensile deformation behavior of superalloy 718 at elevated temperatures, J. Alloys Compd. 471 (2009) 331–335. doi:10.1016/j.jallcom.2008.03.082.

[16] J.-L. Chaboche, P. Kanoute, F. Azzouz, Cyclic inelastic constitutive equations and their impact on the fatigue life predictions, Int. J. Plast. 35 (2012) 44–66.

[17] A. Chamanfar, L. Sarrat, M. Jahazi, M. Asadi, A. Weck, A.K. Koul, Microstructural

Characteristics of Forged and Heat Treated Inconel-718 Disks, Mater. Des. 52 (2013) 791–800.

[18] S.C. Medeiros, Y. Prasad, W.G. Frazier, R. Srinivasan, Microstructural modeling of metadynamic recrystallization in hot working of IN 718 superalloy, Mater. Sci. Eng. A. 293 (2000) 198–207.

[19] L.X. Zhou, T.N. Baker, Effects of strain rate and temperature on deformation behaviour of IN 718 during high temperature deformation, Mater. Sci. Eng. A. 177 (1994) 1–9.

[20] L.A. Reyes, P. Páramo, A.S. Zamarripa, M. de la Garza, M.P.G. Mata, Grain size modeling of a Ni-base superalloy using cellular automata algorithm, Mater. Des. 83 (2015) 301–307.

[21] H.Y. Zhang, S.H. Zhang, Z.X. Li, M. Cheng, Hot die forging process optimization of superalloy IN718 turbine disc using processing map and finite element method, Proc. Inst. Mech. Eng. Part B J. Eng. Manuf. 224 (2010) 103–110.

[22] Y. Wang, L. Zhen, W.Z. Shao, L. Yang, X.M. Zhang, Hot working characteristics and dynamic recrystallization of delta-processed superalloy 718, J. Alloys Compd. 474 (2009) 341–346.

[23] Y. Wang, W.Z. Shao, L. Zhen, X.M. Zhang, Microstructure evolution during dynamic recrystallization of hot deformed superalloy 718, Mater. Sci. Eng. A. 486 (2008) 321–332.

[24] D. Feng, X.M. Zhang, S.D. Liu, Y.L. Deng, Constitutive equation and hot deformation behavior of homogenized Al–7.68Zn–2.12Mg–1.98Cu–0.12Zr alloy during compression at elevated temperature, Mater. Sci. Eng. A. 608 (2014) 63–72. doi:http://dx.doi.org/10.1016/j.msea.2014.04.055.

[25] A.A. Guimaraes, J.J. Jonas, Recrystallization and aging effects associated with the high temperature deformation of Waspaloy and Inconel 718, Metall. Trans. A. 12 (1981) 1655–1666.

[26] Y.-S. Na, J.-T. Yeom, N.-K. Park, J.-Y. Lee, Prediction of microstructure evolution during high temperature blade forging of a Ni− Fe based superalloy, Alloy 718, Met. Mater. Int. 9 (2003) 15–19.

[27] L.X. Zhou, T.N. Baker, Effects of dynamic and metadynamic recrystallization on microstructures of wrought IN-718 due to hot deformation, Mater. Sci. Eng. A. 196 (1995) 89–95.

[28] N. Srinivasan, Y.V.R.K. Prasad, Microstructural control in hot working of IN-718 superalloy using processing map, Metall. Mater. Trans. A. 25 (1994) 2275–2284.

[29] N. Nayan, N.P. Gurao, S.V.S.N. Murty, A.K. Jha, B. Pant, K.M. George, Microstructure and micro-texture evolution during large strain deformation of Inconel alloy IN718, Mater. Charact. (2015).

[30] K. Chen, J. Wu, H. Shi, X. Chen, Z. Shen, M. Zhang, et al., Transition of deformation behavior and its related microstructure evolution in Nimonic 80A under hot-to-warm working, Mater. Charact. 106 (2015) 175–184.

[31] S.M. Fatemi-Varzaneh, A. Zarei-Hanzaki, H. Beladi, Dynamic recrystallization in AZ31 magnesium alloy, Mater. Sci. Eng. A. 456 (2007) 52–57.

[32] M.R.G. Ferdowsi, M. Mazinani, G.R. Ebrahimi, Effects of hot rolling and inter-stage annealing on the microstructure and texture evolution in a partially homogenized AZ91 magnesium alloy, Mater. Sci. Eng. A. 606 (2014) 214–227.

[33] A.S.H. Kabir, M. Sanjari, J. Su, I.-H. Jung, S. Yue, Effect of strain-induced precipitation on dynamic recrystallization in Mg–Al–Sn alloys, Mater. Sci. Eng. A. 616 (2014) 252–259.

[34] Y. Yang, X. Peng, H. Wen, B. Zheng, Y. Zhou, W. Xie, et al., Influence of extrusion on the microstructure and mechanical behavior of Mg-9Li-3Al-xSr alloys, Metall. Mater. Trans. A. 44 (2013) 1101–1113.

[35] L. Donati, A. Segatori, M. El Mehtedi, L. Tomesani, Grain evolution analysis and experimental validation in the extrusion of 6XXX alloys by use of a lagrangian FE code, Int. J. Plast. 46 (2013) 70–81.

[36] Y.C. Lin, X.-Y. Wu, X.-M. Chen, J. Chen, D.-X. Wen, J.-L. Zhang, et al., EBSD study of a hot deformed nickel-based superalloy, J. Alloys Compd. 640 (2015) 101–113.

[37] H. Jiang, J. Dong, M. Zhang, Z. Yao, Evolution of twins and substructures during low strain rate hot deformation and contribution to dynamic recrystallization in alloy 617B, Mater. Sci. Eng. A. 649 (2016) 369–381.

[38] Q. Guo, D. Li, S. Guo, H. Peng, J. Hu, The effect of deformation temperature on the microstructure evolution of Inconel 625 superalloy, J. Nucl. Mater. 414 (2011) 440–450. doi:10.1016/j.jnucmat.2011.05.029.

[39] Y. Cao, H. Di, J. Zhang, J. Zhang, T. Ma, R.D.K. Misra, An electron backscattered diffraction study on the dynamic recrystallization behavior of a nickel – chromium alloy (800H) during hot deformation, Mater. Sci. Eng. A. 585 (2013) 71–85. doi:10.1016/j.msea.2013.07.037.

[40] H. Zhang, K. Zhang, H. Zhou, Z. Lu, C. Zhao, X. Yang, Effect of strain rate on microstructure evolution of a nickel-based superalloy during hot deformation, Mater. Des. 80 (2015) 51–62.

[41] N. Shkatulyak, Effect of stacking fault energy on the mechanism of texture formation during alternating bending of FCC metals and alloys, Int. J. Nonferrous Metall. 2 (2013). doi:10.4236/ijnm.2013.22005.

[42] Z. Wu, C.M. Parish, H. Bei, Nano-twin mediated plasticity in carbon-containing FeNiCoCrMn high entropy alloys, J. Alloys Compd. 647 (2015) 815–822.

[43] M. Azarbarmas, M. Aghaie-Khafri, J.M. Cabrera, J. Calvo, Microstructural evolution and constitutive equations of Inconel 718 alloy under quasi-static and quasi-dynamic conditions, Mater. Des. 94 (2016) 28–38.

[44] E.S. Puchi-Cabrera, M.H. Staia, J.D. Guérin, J. Lesage, M. Dubar, D. Chicot, An experimental analysis and modeling of the work-softening transient due to dynamic recrystallization, Int. J. Plast. 54 (2014) 113–131.

[45] E.I. Galindo-Nava, P.E.J. Rivera-Díaz-del-Castillo, Thermostatistical modelling of hot deformation in FCC metals, Int. J. Plast. 47 (2013) 202–221.

[46] J. Hajkazemi, A. Zarei-Hanzaki, M. Sabet, S. Khoddam, Double-hit compression behavior

of TWIP steels, Mater. Sci. Eng. A. 530 (2011) 233–238.

[47] S.S. Satheesh Kumar, T. Raghu, P.P. Bhattacharjee, G. Appa Rao, U. Borah, Constitutive modeling for predicting peak stress characteristics during hot deformation of hot isostatically processed nickel-base superalloy, J. Mater. Sci. 50 (2015) 6444–6456. doi:10.1007/s10853-015-9200-0.

[48] X.-M. Chen, Y.C. Lin, M.-S. Chen, H.-B. Li, D.-X. Wen, J.-L. Zhang, et al., Microstructural evolution of a nickel-based superalloy during hot deformation, Mater. Des. 77 (2015) 41–49.

[49] P. Zhang, C. Hu, C. Ding, Q. Zhu, H. Qin, Plastic deformation behavior and processing maps of a Ni-based superalloy, Mater. Des. 65 (2015) 575–584.

[50] Y. Kong, P. Chang, Q. Li, L. Xie, S. Zhu, Hot Deformation Characteristics and Processing Map of Nickel-Based C276 Superalloy, J. Alloys Compd. (2014).

[51] A.A. Brown, D.J. Bammann, Validation of a model for static and dynamic recrystallization in metals, Int. J. Plast. 32 (2012) 17–35.

[52] O.N. Senkov, D.B. Miracle, S.A. Firstov, Metallic materials with high structural efficiency, Springer Science & Business Media, 2006.

[53] S.M. Fatemi-Varzaneh, A. Zarei-Hanzaki, J.M. Cabrera, P.R. Calvillo, EBSD characterization of repetitive grain refinement in AZ31 magnesium alloy, Mater. Chem. Phys. 149 (2015) 339–343.

[54] Z. Yanushkevich, A. Belyakov, R. Kaibyshev, Microstructural evolution of a 304-type austenitic stainless steel during rolling at temperatures of 773–1273K, Acta Mater. 82 (2015) 244–254.

[55] M.G. Jiang, H. Yan, R.S. Chen, Twinning, recrystallization and texture development during multi-directional impact forging in an AZ61 Mg alloy, J. Alloys Compd. 650 (2015) 399–409.

[56] R. Jamaati, M.R. Toroghinejad, S. Amirkhanlou, H. Edris, Microstructural evolution of nanostructured steel-based composite fabricated by accumulative roll bonding, Mater. Sci. Eng. A. 639 (2015) 298–306.

[57] S.R. Barrabes, M.E. Kassner, M.T. Pérez-Prado, E. Evangelista, Geometric Dynamic Recrystallization in α-Zirconium at Elevated Temperatures, in: Mater. Sci. Forum, Trans Tech Publ, 2004: pp. 1145–1150.

[58] S.M. Schmid, M. Casey, J. Starkey, An illustration of the advantages of a complete texture analysis described by the orientation distribution function (ODF) using quartz pole figure data, Tectonophysics. 78 (1981) 101–117.

[59] Y.J. Chen, Y.J. Li, J.C. Walmsley, S. Dumoulin, H.J. Roven, Deformation structures of pure titanium during shear deformation, Metall. Mater. Trans. A. 41 (2010) 787–794.

[60] M.G. Shahri, S.R. Hosseini, M. Salehi, Formation of Nano/Ultrafine Grains in AISI 321 Stainless Steel Using Advanced Thermo-Mechanical Process, Acta Metall. Sin. (English Lett. 28 (2015) 499–504.

[61] S.M.A. Khan, H.M. Zbib, D.A. Hughes, Modeling planar dislocation boundaries using multi-scale dislocation dynamics plasticity, Int. J. Plast. 20 (2004) 1059–1092.

doi:http://dx.doi.org/10.1016/j.ijplas.2003.10.004.

[62] D. Bombac, M.J. Peet, S. Zenitani, S. Kimura, T. Kurimura, H. Bhadeshia, An integrated hot rolling and microstructure model for dual-phase steels, Model. Simul. Mater. Sci. Eng. 22 (2014) 45005.

[63] O. Nishikawa, K. Saiki, H.-R. Wenk, Intra-granular strains and grain boundary morphologies of dynamically recrystallized quartz aggregates in a mylonite, J. Struct. Geol. 26 (2004) 127–141.

[64] S. Shekhar, A.H. King, Strain fields and energies of grain boundary triple junctions, Acta Mater. 56 (2008) 5728–5736. doi:http://dx.doi.org/10.1016/j.actamat.2008.07.053.

[65] T. Yu, N. Hansen, X. Huang, Recovery by triple junction motion in aluminium deformed to ultrahigh strains, in: Proc. R. Soc. London A Math. Phys. Eng. Sci., The Royal Society, 2011: pp. 3039–3065.

[66] P.R. Rios, F. Siciliano Jr, H.R.Z. Sandim, R.L. Plaut, A.F. Padilha, Nucleation and growth during recrystallization, Mater. Res. 8 (2005) 225–238.

[67] A.A. Saleh, A.A. Gazder, E. V Pereloma, EBSD observations of recrystallisation and tensile deformation in twinning induced plasticity steel, Trans. Indian Inst. Met. 66 (2013) 621–629.

[68] R. Jones, V. Randle, D. Engelberg, T.J. Marrow, Five-parameter grain boundary analysis of a grain boundary–engineered austenitic stainless steel, J. Microsc. 233 (2009) 417–422.

[69] S.T. Downey II, N. Bembridge, P.N. Kalu, H.M. Miller, G.S. Rohrer, K. Han, Grain boundary plane distributions in modified 316 LN steel exposed at elevated and cryogenic temperatures, J. Mater. Sci. 42 (2007) 9543–9547.

[70] B. Raj, Materials and manufacturing technologies for sodium cooled fast reactors and associated fuel cycle: innovations and maturity, Energy Procedia. 7 (2011) 186–198.

[71] W. Wang, S. Lartigue-Korinek, F. Brisset, a. L. Helbert, J. Bourgon, T. Baudin, Formation of annealing twins during primary recrystallization of two low stacking fault energy Ni-based alloys, J. Mater. Sci. 50 (2014) 2167–2177. doi:10.1007/s10853-014-8780-4.

[72] Z. Li, L. Zhang, N. Sun, Y. Sun, A. Shan, Effects of prior deformation and annealing process on microstructure and annealing twin density in a nickel based alloy, Mater. Charact. 95 (2014) 299–306.

[73] H. Beladi, P. Cizek, P.D. Hodgson, Dynamic recrystallization of austenite in Ni-30 Pct Fe model alloy: microstructure and texture evolution, Metall. Mater. Trans. A. 40 (2009) 1175–1189.

[74] F.J.Humphreys, M.Hatherly, Recrystallization And Related Annealing Phenomena, 2nd editio, 2004.

[75] M. Aghaie-Khafri, R. Mahmoudi, Optimizing homogenization parameters for better stretch formability in an Al–Mn–Mg alloy sheet, Mater. Sci. Eng. A. 399 (2005) 173–180.

[76] C. Roberts, Grain growth and the Zener pinning phenomenon: A computational and experimental investigation, ProQuest, 2008.